

Radiative Energy Budget in the Cloudy and Hazy Arctic

SI-CHEE TSAY

Geophysical Institute and Department of Physics, University of Alaska-Fairbanks, Fairbanks, Alaska

KNUT STAMNES*

The Auroral Observatory, Institute of Mathematical and Physical Sciences, University of Tromsø, N-9001, Tromsø, Norway

KOLF JAYAWEERA

Department of Physics, University of Alaska-Fairbanks, Fairbanks, Alaska

(Manuscript received 25 February 1988, in final form 18 October 1988)

ABSTRACT

A radiation model is constructed that includes radiative interactions with atmospheric gases, as well as parameterized treatments of scattering and absorption/emission by cloud droplets and haze particles. A unified treatment of solar and terrestrial radiation is obtained by using identical cloud and haze parameterization procedure for the shortwave and longwave region. The influence of the relative humidity of the haze particles is also considered. Snow conditions of the arctic region are simulated in terms of snow grain sizes and soot contamination in the surface layers. Data from the Arctic Stratus Cloud Experiment collected in 1980 are used for model comparisons and sensitivity studies under cloudy and hazy sky conditions.

During the arctic summer, stratus clouds are a persistent feature and decrease the downward flux at the surface by about $130\text{--}200\text{ W m}^{-2}$. Arctic haze in the summertime is important if it is above the cloud layer or in air with low relative humidity, and it decreases the downward flux at the surface by about $10\text{--}12\text{ W m}^{-2}$. By comparison the greenhouse effect of doubling the carbon dioxide amount increases the downward flux at the surface by about $4\text{--}7\text{ W m}^{-2}$ and can be offset by the background haze or by an increase in cloudiness of about 4%.

Assuming steady microstructures of stratus clouds, we find that in late June a clear sky condition results in more available downward flux for snow melt (yielding a melting rate of 9.3 cm day^{-1}) than does a cloudy sky condition (6 cm day^{-1}). This is because the increase of infrared radiation diffused back to the surface by the cloud can not compensate for the reduction of solar radiation. When the snow starts to melt, the decreasing snow albedo further accelerates the melting process.

1. Introduction

Energy is transported between the earth-atmosphere system and space by radiation. Due to the alignment of the sun-earth system, there is a radiation surplus in the equatorial region and a radiation deficit in both polar areas. Therefore, the Arctic plays a very important role in the energy exchange process. One of the dominant factors modulating the radiation budget and the energy exchange process is the presence of clouds. Generally, the high albedo of clouds results in a cooling of the earth-atmosphere system, because of the low background reflectivity. This cooling effect, however, may be much less pronounced in the Arctic where the background albedo is higher due to snow/ice cover.

During the summer, low-level stratiform clouds are a prevalent feature in the Arctic. These clouds are commonly overlying a snow/ice covered surface with albedo of about 0.6–0.8. Since the sun never sets in the arctic summer, these clouds are illuminated at a relatively low solar elevation (maximum 47° above the horizon at local solar noon at the summer solstice), which increases the cloud optical path length. When the cloud becomes optically thick and thus prevents photon penetration, the multiple reflection between the cloud and snow/ice surface is diminished. The albedo of the cloud-atmosphere-surface system is dominated by the cloud albedo itself (about 0.5–0.7), which is comparable to or less than that of snow/ice. Thus the presence of clouds, in this case, may change the usual cooling effect to a slight heating of the surface-atmosphere system. Figure 1, for example, shows that clouds are viewed darker than the background snow/ice in the Beaufort sea in visible satellite imagery.

Recent comprehensive compilations of global cloud type and amount by Warren et al. (1988) indicate that

* Present affiliation: Geophysical Institute and Department of Physics, University of Alaska, Fairbanks, AK 99775-0800.

Corresponding author address: Dr. Si-Chee Tsay, Dept. of Atmospheric Science, Colorado State University, Ft. Collins, CO 80523.



FIG. 1. Satellite picture in visible channel of the Beaufort sea (a) cloud, (b) open leads, (c) snow/ice covered surface and (d) Alaska coast line.

maritime stratiform clouds has about 34% coverage over the ocean (or roughly 25% coverage of the globe) in the summer season. The Arctic Ocean occupies about 4% of the global area. About 70% of the Arctic Ocean is often covered by stratus clouds (Huschke 1969; Vowinckel and Orvig 1970), implying that the arctic stratus contributes about 3% to the global coverage. Since the areal coverage of the Arctic is relatively low, the potential influence of the Arctic on the global climate is often neglected, despite the contribution of 12% (3% vs 25%) in cloud amount by the arctic stratus. Moreover, the coupling of arctic stratus with the high surface albedo of the Arctic region plays an important role in climatic feedback mechanisms (Kellogg 1975). A small perturbation in the cloud amount may produce a large amplification in radiation-climate interaction. Therefore, sensitivity studies of the radiative properties of the arctic stratus are of fundamental importance for understanding the radiative energy exchange in the Arctic.

The arctic stratus clouds tend to occur in the boundary layer (within 2 km of height) and are frequently

observed to be laminated or comprised of two or more separate, well-defined layers (Jayaweera and Ohtake 1973; Herman 1977). A more detailed description of the physical characteristics of the arctic stratus is given by Tsay and Jayaweera (1984). It has long been noted that the morphology of the arctic stratus facilitates theoretical radiative transfer studies in plane-parallel geometry with multiple scattering (Feigelson 1964; Wiscombe 1975; Herman and Goody 1976); but the dependence of the radiative properties of these clouds on their microstructure was only recently considered (Tsay et al. 1983; Herman and Curry 1984). Furthermore, profiles of radiative fluxes and heating/cooling rates have not been examined in the Arctic. Previous studies have focused on the bulk radiative quantities such as ratios of fluxes and/or flux divergences (e.g. reflectivity and absorptivity). In this paper we compute the flux and heating/cooling profiles to gain insight into the vertical distribution of the atmospheric radiation energy.

In section 2 we describe the construction and parameterization of a comprehensive radiation model,

including atmospheric scattering, absorption and emission by molecules as well as particulate matter, under the summertime arctic boundary conditions of long solar insolation and high surface albedo. In section 3 we first test the model performance against the measured fluxes and bulk radiative quantities. We then proceed in section 4 to conduct a sensitivity study of the effects of cloud, haze and snow on the radiative energy budget of the arctic atmosphere and surface to obtain a better understanding of the role of radiation in the climate of the Arctic. A summary of this study is given in section 5.

2. Description of radiation model

a. Basic equations and solutions

In this paper we focus on the computation of heating/cooling rates for which only fluxes are needed. Thus, we may start with the azimuthally averaged version of the equation describing the transfer of diffuse monochromatic radiation at frequency ν in a scattering, absorbing and emitting plane-parallel atmosphere in local thermodynamic equilibrium given by (Chandrasekhar 1960; Stamnes et al. 1988)

$$\begin{aligned} \mu \frac{du_\nu(\tau_\nu, \mu)}{d\tau_\nu} &= u_\nu(\tau_\nu, \mu) - \frac{\omega_\nu(\tau_\nu)}{4\pi} \\ &\times \int_{-1}^1 P_\nu(\tau_\nu, \mu; \mu') u_\nu(\tau_\nu, \mu') d\mu' - \frac{\omega_\nu(\tau_\nu) I_0}{4\pi} \\ &\times P_\nu(\tau_\nu, \mu; -\mu_0) e^{-\tau_\nu/\mu_0} - [1 - \omega_\nu(\tau_\nu)] B_\nu(T). \end{aligned} \quad (1)$$

Here θ is the polar angle and $\mu = \cos\theta$. We have made the usual diffuse-direct distinction (Chandrasekhar 1960, p. 22) so that u_ν in Eq. (1) describes the azimuthally averaged diffuse intensity or radiance only. Thus, I_0 is the intensity of solar radiance incident in direction μ_0 so that $\mu_0 I_0$ is the incident vertical flux or irradiance. The $\omega_\nu(\tau_\nu)$ is the single scattering albedo, $P_\nu(\tau_\nu, \mu; \mu')$ the azimuthally averaged scattering phase function, τ_ν the extinction optical depth and $B_\nu(T)$ the Planck function at frequency ν and temperature T . The second term on the right side in Eq. (1) is due to multiple scattering, the third is a consequence of the diffuse-direct distinction and is called the solar pseudosource, while the fourth term describes thermal emission.

Since planetary atmospheres, in general, and the earth's atmosphere, in particular, consists of a mixture of various radiatively active gases and cloud and aerosol particles that have nonconstant mixing ratios, the optical properties (i.e. the single scattering albedo and the phase function) vary with altitude or optical depth. To account for this inhomogeneity and the fact that real atmospheres are nonisothermal, we divide the atmosphere into a series of adjacent, homogeneous layers in which the scattering and absorbing properties are taken to be constant within each layer but are allowed

to vary from layer to layer. Within each layer we adopt a linear-in-optical-depth variation of the Planck function (Wiscombe 1976).

A variety of techniques exist for solving Eq. (1) (cf. Stamnes 1986 for a recent review of such methods). Applying the discrete ordinate method (Stamnes et al. 1988) we find that the intensity for layer denoted by p is given by

$$\begin{aligned} u_p(\tau, \mu_i) &= \sum_{j=1}^N \{ C_{jp} G_{jp}(\mu_i) e^{-k_{jp}(\tau - \tau_{p-1})} \\ &+ C_{-jp} G_{-jp}(\mu_i) e^{-k_{jp}(\tau_p - \tau)} \} + Z_p(\mu_i) e^{-\tau/\mu_0} \\ &+ [Y_{0p}(\mu_i) + Y_{1p}\tau], \end{aligned} \quad (2)$$

where the μ_i are the quadrature angles and $\tau_{p-1} \leq \tau \leq \tau_p$; N is the number of discrete points utilized in each hemisphere when replacing the integral over angle in Eq. (1) by numerical quadrature. The k_{jp} and $G_{jp}(\mu_i)$ are the eigenvalues and eigenvectors, respectively, which depend on the optical properties of each layer. The C_{jp} are determined from boundary and continuity conditions and depend upon the incident solar radiation, the atmospheric thermal properties and the surface characteristics, $Z_p(\mu_i) \exp(-\tau/\mu_0)$ is the particular solution due to a parallel beam of solar radiation incident in direction $\theta_0 = \cos^{-1}\mu_0$. The $Y_{0p}(\mu_i)$ and Y_{1p} are determined by the optical and thermal properties of the layer. We refer the reader to a recent paper (Stamnes et al. 1988) for a complete and detailed account of this method.

To compute fluxes and heating/cooling rates we use the formulas

$$\begin{aligned} F_\nu(\tau_\nu) &= \int_0^{2\pi} d\phi \int_{-1}^1 \mu u_\nu(\tau_\nu, \mu) d\mu \\ &= 2\pi \sum_{i=-N}^N w_i \mu_i u_\nu(\tau_\nu, \mu_i) \end{aligned} \quad (3)$$

$$\frac{\partial T}{\partial t} = -\frac{1}{C_p \rho} \frac{\partial F_\nu}{\partial z}, \quad (4)$$

where ϕ refers to the integration over azimuths; w_i is the quadrature weight; T stands for temperature, t for time, C_p for specific heat at constant pressure p , ρ for mass density, z for geometric height and F_ν for net flux at frequency ν . The heating/cooling rate is proportional to the divergence of the net flux.

b. Parameterization of molecular scattering and absorption/emission

Figure 2a, modified from Coulson (1975) and Liou (1980), shows an overall picture of the clear sky radiation. For convenience it has been customary to separate solar and terrestrial radiation at $4 \mu\text{m}$ because of the negligible amounts of energy existing on either side of $4 \mu\text{m}$ for each relative to the other. For solar radia-

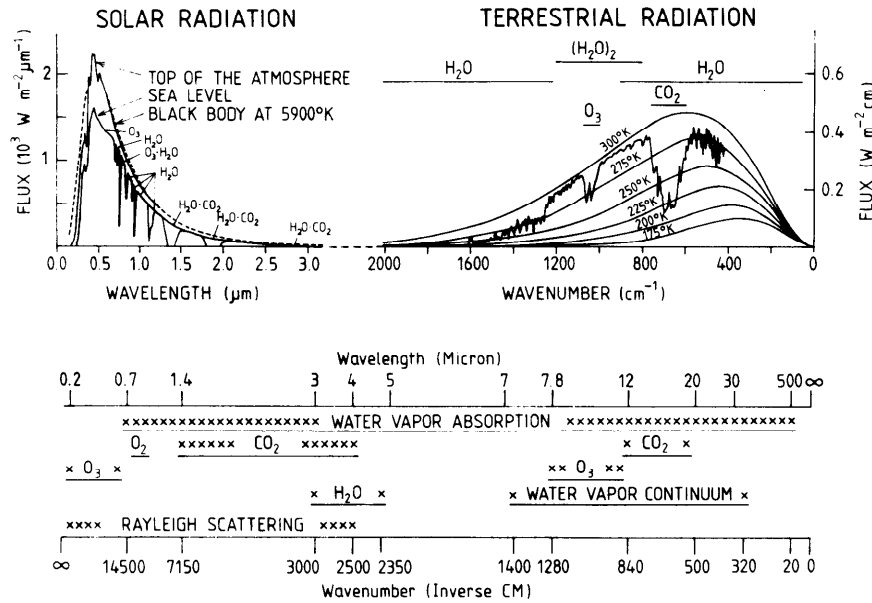


FIG. 2. (a) Spectral distribution of gaseous scattering and absorption/emission for two clear-sky observations (modified from Coulson 1975 and Liou 1980). (b) Spectral distribution for exponential-sum fitting of transmission for gaseous absorption/emission.

tion, the outer curve in Fig. 2a was observed at the top of the atmosphere while the inner curve was observed at sea level. The area between the inner and the outer curve is due to molecular and aerosol scattering and absorption. For terrestrial radiation (note that the vertical scale is different), the emission spectrum was observed by satellite interferometer from space.

Due to the small amount of energy involved in transitions from one quantum state to another, the gaseous rotational/vibrational absorption spectra consist essentially of complex, closely spaced line structures. The necessary spectral line parameters (e.g. frequency at line center, intensity, half-width) have been compiled and reported by McClatchey et al. (1973) and continuously updated since then to include some 159 000 lines (Rothman 1981). The difficulty involved in incorporating either fine line structure (e.g. time-consuming computations) or broadband measurement absorption data (e.g. varying temperature and pressure profiles) into multiple scattering radiation models has been discussed recently by Chou and Arking (1980, 1981), Slingo and Schrecker (1982) and Stephens (1984) among others. Therefore, parameterization of gaseous absorption over a spectral region containing many lines is needed for computational efficiency when absorption is included in a multiple scattering scheme. For this purpose, we have adopted the exponential-sum fitting of transmissions (ESFT) method described briefly below.

The ESFT method approximates the transmission function of a given spectral region by a finite sum of M exponential terms (Wiscombe and Evans 1977), as follows:

$$\tilde{T}(u) \equiv \sum_{i=1}^M w_i e^{-b_i u} \quad (5)$$

where $\sum_{i=1}^M w_i = 1$. Here, \tilde{T} denotes the band transmission

function and u is the equivalent absorber amount. The b_i are the equivalent absorption coefficients and the w_i are associated weights ($b_i \geq 0$, $w_i > 0$). In essence, the main virtue of the ESFT method is to reduce the non-gray radiative transfer problem involving integration over a finite spectral interval (for which Beer's law does not apply) to a series of monochromatic problems. Figure 2b shows the spectral regions in which the four gases, considered in this study, absorb radiant energy. The ESFT method is used to deal with each gas in the wavelength interval from 0.3 to 500 μm . Two different ESFT data sets have kindly been provided to us by Dr. Wiscombe (1985, personal communication) and by Drs. Slingo and Schrecker (1982). For terrestrial radiation we have used the former data set which has a resolution of 20 cm^{-1} and accounts for overlapping gaseous absorption. For solar radiation we have adopted the latter data set which has irregular spectral resolution.

Empirical scaling of absorber amounts (u_0) is needed to account for the pressure and temperature dependence. Thus, the effective absorber amount (u) is obtained as follows:

$$u(z) = u_0(z) \left\{ \frac{p(z)}{p(0)} \left[\frac{T(0)}{T(z)} \right]^{1/2} \right\}^n \quad (6)$$

where $p(0) = 1013.25$ mb; $T(0) = 273.15$ K; and the

constant n is determined empirically to be 0.9 for H_2O , 0.75 for the uniformly mixed gases (CO_2 and O_2), and 0.4 for O_3 (Kneizys et al. 1980).

Besides molecular absorption, Rayleigh scattering is important in the spectral region from 0.3 to 4.0 μm , due to the dependence of scattered radiation on λ^{-4} (λ , monochromatic wavelength). We have adopted Penndorf's (1957) formula for the Rayleigh's volume scattering coefficient (β_R , m^{-1}) given by

$$\beta_R(z) = [0.9793(n_a^2 - 1)^2 p(z)] / [\lambda^4 T(z)] \quad (7)$$

where n_a denotes the refractive index of air and temperature and pressure dependence is also taken into account.

c. Parameterization of atmospheric particles and surface conditions

Important parameters for multiple scattering problems involving particles are the single scattering albedo (ω , or the probability of scattering), the optical depth (τ , determined by the extinction coefficient along the path), and the asymmetry factor (g , characterizing the angular scattering pattern). Due to instrumental limitations, these three dimensionless optical properties are difficult to measure directly in the laboratory (e.g., Mugnai and Wiscombe 1980). Mie theory is often the most suitable method to obtain these quantities, but unfortunately Mie computations are very time-consuming. For computational expediency it is therefore convenient to utilize Mie theory to parameterize the optical properties of stratus clouds, arctic haze and snow/ice particles in terms of their bulk microphysical properties, such as size distribution and mass content, which can be measured directly.

1) STRATUS CLOUDS

The microphysics of clouds may be conveniently described by the liquid water content (LWC, g cm^{-3}), the equivalent radius (RE, μm), and the total number concentration (CON, cm^{-3}) as follows:

$$\begin{aligned} \text{LWC}(z) &= \frac{4\pi\rho_w}{3} \int r^3 n(r, z) dr \\ \text{RE}(z) &= \frac{\int r^3 n(r, z) dr}{\int r^2 n(r, z) dr} \\ \text{CON}(z) &= \int n(r, z) dr \end{aligned} \quad (8)$$

where ρ_w (g cm^{-3}) is the density of water, r (μm) is the droplet radius and $n(r, z)$ ($\text{cm}^{-3} \mu\text{m}^{-1}$) is the drop size distribution at height z . Based on the extensive survey of cloud microphysics by Carrier et al. (1967), Stephens (1978) established eight cloud models which

cover a wide range of observed drop size distributions. A tabulation of the optical properties of these eight water clouds was also made by Stephens (1979) through Mie computations from 0.3 to 200 μm . Since cumulus and cumulonimbus are cube-shaped clouds which have characteristics very different from stratiform clouds, these two model size distributions are not appropriate for this study. Moreover, even for the stable and stratiform clouds, such as the arctic stratus, different size distributions were observed from cloud base to top. In fact, a single-mode size distribution was often found near the cloud base; but the shape of the size spectrum shifted toward larger size at the upper levels and a bimodal distribution was observed near the cloud top (cf. Fig. 10 of Tsay and Jayaweera 1984). The arctic stratus has microphysical properties (RE, LWC and CON) somewhat between those of the marine stratocumulus (SC-II) and the stratus (ST-II) identified by Stephens (1978). Therefore, a multimode size distribution (having the same LWC and CON as SC-II) was simulated to resemble the distribution at cloud top. Figure 3 shows the SC-II and the adopted multimode size distributions. Mie computations were performed for the multimode size distribution to obtain its optical properties and this model cloud combined with the six clouds of Stephens (1979), deemed appropriate for our purposes, serve as a basis for our parameterization of stratiform clouds.

To demonstrate the relationship between cloud microphysics and cloud optical properties, we show in Fig. 4 the single scattering albedo for solar and terrestrial spectra. If the ST-II and the multimode clouds serve as the envelope, based on the rank of RE, the rest of the five model clouds are generally bounded

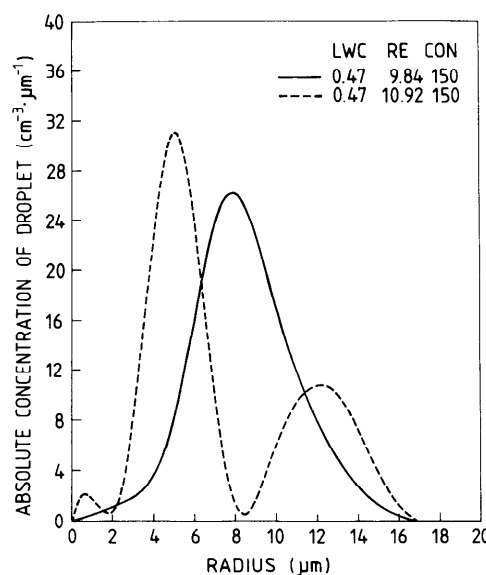


FIG. 3. Drop size distributions for two model clouds (solid: for single-mode and dashed: for multi mode SC-II, see text).

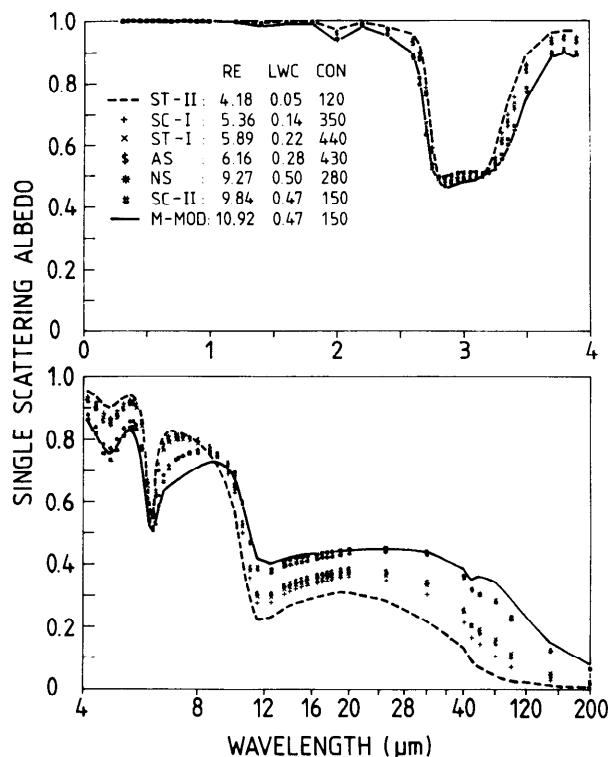


FIG. 4. Single scattering albedo for seven model clouds from wavelength 0.3 to 200 μm .

inside. Recent studies have attempted to parameterize shortwave optical properties, based on one or two bulk quantities of cloud microphysics (Stephens 1978; Twomey and Bohren 1980; Slingo and Schrecker 1982; Wiscombe et al. 1984). To obtain a unified treatment of both solar and terrestrial radiation, an extension of Slingo and Schrecker's parameterization scheme for the solar spectrum is attempted here for the terrestrial spectrum as well. Since ω and g are ratios of two quantities, they depend closely on RE, which is the ratio of the third and the second moments of size distribution. The extinction coefficient β_{ext} depends on LWC/RE, which represents the total cross section. Therefore, to parameterize the optical properties we performed least squares fits for the following linear equations for the wavelength region from 0.3 to 200 μm :

$$\omega = a + b\text{RE}$$

$$g = c + d\text{RE}$$

$$\beta_{\text{ext}}/\text{LWC} = e + f/\text{RE}. \quad (9)$$

Figures 5–7 show each 12 representative wavelength fits out of a total of 120 for ω , g and weighted extinction coefficient ($\beta_{\text{ext}}/\text{LWC}$). A good fit for ω throughout the solar and terrestrial spectra is obtained. Very high absolute values of correlation coefficients (γ) are found. This is very important for cloud parameterization, because cloud absorption is very sensitive to the variation

of $(1 - \omega)$. The fits for g are also good, except for the region around 4.5 μm . However, this error may not produce serious problems, due to the relatively small amount of radiation energy involved. Good fits of weighted β_{ext} were obtained for both the shortwave and longwave regions. Relatively low correlation coefficients were obtained only in the window region (8–12 μm).

2) ARCTIC HAZE

Besides the persistent summertime arctic stratus, the presence of aerosol particles in the arctic atmosphere has received attention in recent years because of possible climatic effects. Arctic haze has a seasonal variation with a maximum in late spring and a minimum in late summer (Patterson et al. 1982; Shaw 1982), and tends to occur in multiple layers rather than being well mixed throughout the lower atmosphere (Carlson 1981; Valero et al. 1983). The layering of the haze often occurs within 3 km above the surface, which is about the upper height limit for the summertime arctic stratus cloud. The low concentration of arctic haze during the summer season may be related to the high occurrence of stratus clouds. The optical properties (β_{ext} , ω , g) of arctic haze have not been extensively

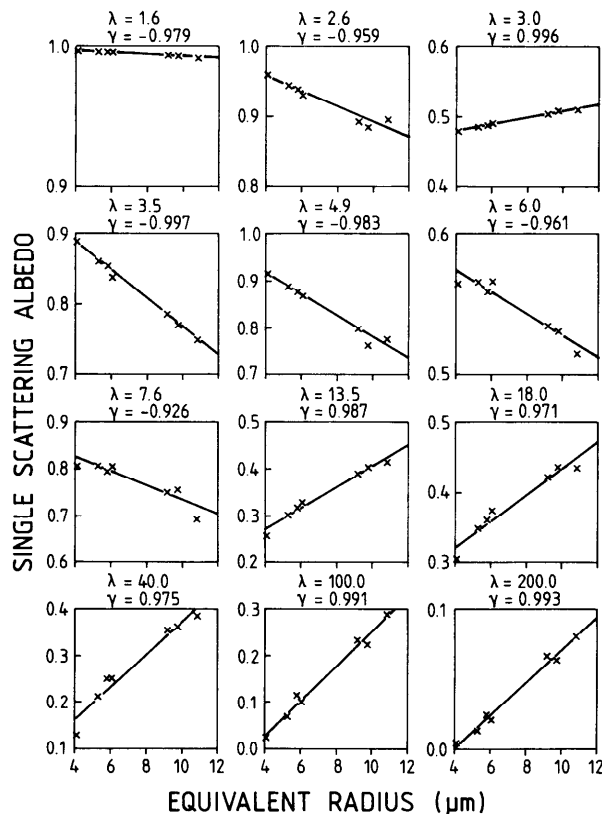


FIG. 5. Least squares fits of single scattering albedo from wavelength 0.3 to 200 μm for seven cloud models (λ denotes wavelength and γ correlation coefficient).

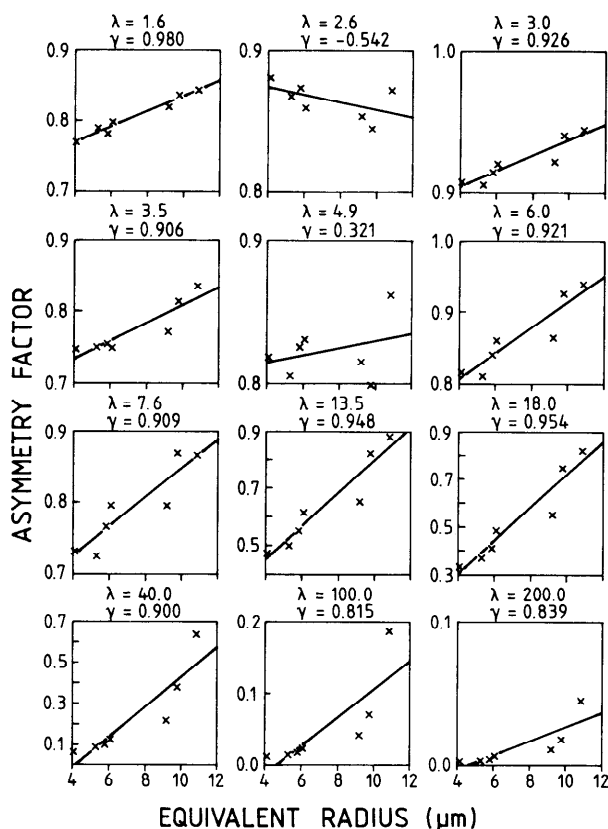


FIG. 6. As in Fig. 5, except for asymmetry factor.

measured (Shaw 1985); however, reported values exist only at a few single wavelengths (e.g., 500 nm). To estimate the effect of haze on the radiative energy budget in the Arctic, the wavelength dependence of the optical properties is essential. Therefore, Mie calculations again may provide estimates of the optical properties, based on the measured microphysics of the haze.

Recent model computations of the optical properties for aerosol particles were made by Shettle and Fenn (Tables 12–43, 1979) and Blanchet and List (Figs. 10–12, 1983). The former compilation contains four general models of aerosols; the latter applies specifically for arctic haze. Figure 8 shows β_{ext} for both model calculations. Effects of humidity on the aerosol properties are considered in both models. The volume extinction coefficient of arctic haze is generally of the same order of magnitude as that of the tropospheric aerosols rather than that of the maritime aerosols. A background haze of optical depth ranging from 0.05 to 0.2 is chosen for the summertime arctic condition (Shaw 1985).

Dry (relative humidity $\leq 80\%$) and wet ($RH > 80\%$) conditions represent cases of haze particles located above/below and inside the clouds, respectively. Since haze particles lose their optical characteristics quickly as they get wet (acting as a tiny droplet), we performed least squares fits for both dry and wet particles. Figure

9 shows 12 representative fits out of a total of 54 cases of RH vs ω from wavelength 0.3 to 40 μm . Very good fits are found in the visible region, which is quite important because the major absorption by haze (dry) occurs here.

When the atmosphere contains a mixture of gas molecules and particulate matter, the effective optical properties of this mixture can be obtained as follows:

$$\tau_{eff} = \tau_G + \tau_R + \tau_D + \tau_H$$

$$\omega_{eff} = (\tau_R + \omega_D \tau_D + \omega_H \tau_H) / \tau_{eff}$$

$$P_{eff}(\cos\Theta)$$

$$= \frac{\tau_R P_R(\cos\Theta) + \omega_D \tau_D P_D(\cos\Theta) + \omega_H \tau_H P_H(\cos\Theta)}{\tau_R + \omega_D \tau_D + \omega_H \tau_H} \quad (10)$$

where the subscripts G , R , D and H denote the components for gaseous absorption, Rayleigh scattering, droplets and haze particles, respectively. Since our interest here lies primarily in the radiative energy balance, we focus on flux computations for which the asymmetry factor is the most important moment of the phase function. To circumvent lengthy computations of phase function moments we utilize the Henyey-Greenstein phase function given by

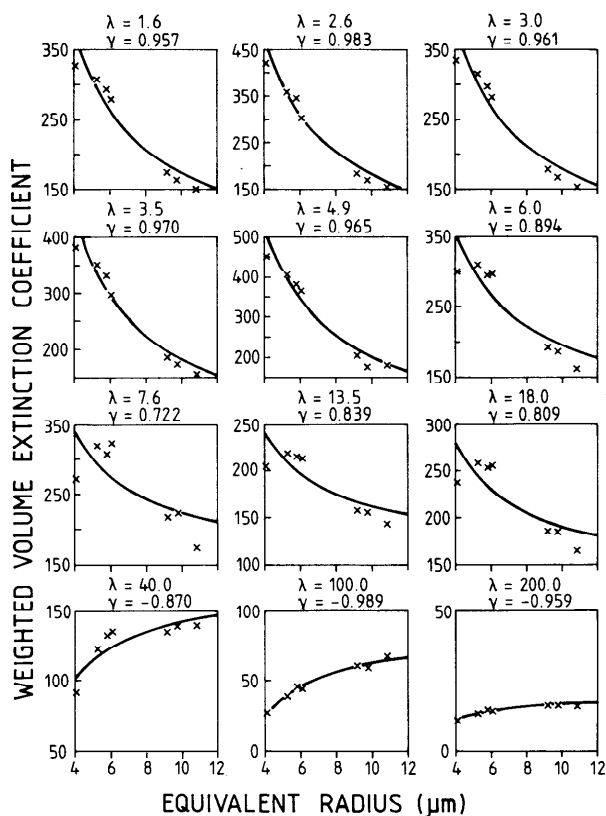


FIG. 7. As in Fig. 5, except for weighted volume extinction coefficient.

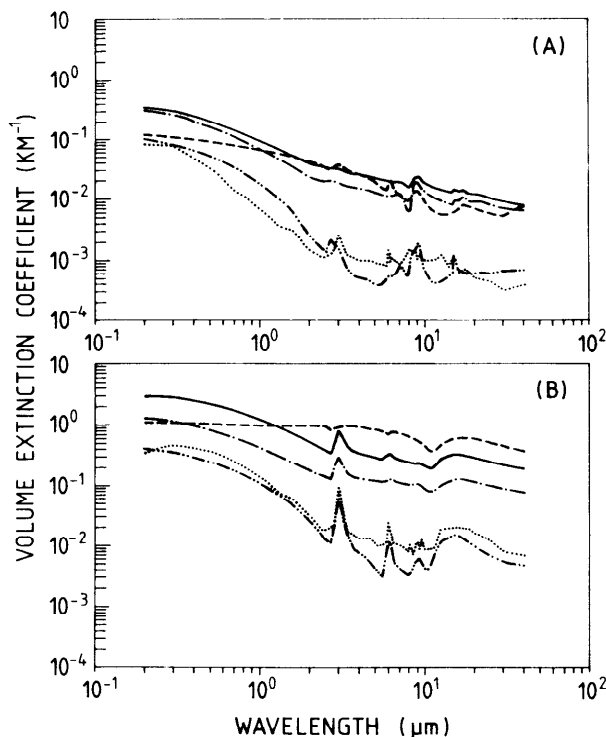


FIG. 8. Volume extinction coefficient for five haze models from wavelength 0.2 to 40 μm at (A) 50% and (B) 99% relative humidity (solid: Urban, dot-dash: Rural, dash: Maritime, dash-double dot: Tropospheric, and dotted: Arctic haze models).

$$P_{\text{HG}}(\cos\theta) = (1 - g^2)/(1 + g^2 - 2g \cos\theta)^{3/2}, \quad (11)$$

where g is the asymmetry factor, since its moments are given simply by powers of g (van de Hulst 1957; Hansen and Travis 1974).

3) SNOW/ICE COVERED SURFACE

The striking feature of the arctic surface is its high reflectivity, caused mainly by snow and sea ice. The surface radiative energy budget depends strongly on its albedo. A high snow/ice albedo produces a positive climatic feedback mechanism, by which an increase in surface albedo leads to more energy reflected to space. Thus, there is less energy available for heating, implying a temperature decrease which induces further extension of snow/ice (Kellogg 1975). To obtain a quantitative understanding of this feedback mechanism, the optical properties of snow/ice have to be known.

However, the snow/ice albedo is generally not a constant, it depends on the wavelength of the incident solar radiation, snow/ice age and depth, air bubble distribution, sun angle, cloud cover, and impurities such as dust, ash, soot, salt (Warren 1982), which creates a difficulty in parameterization. Nevertheless, the most important variable controlling snow/ice albedo turns out to be the mean grain size, which is proportional to the ratio of volume to surface. In general, the

grain radius (RG) varies with snow/ice depth and age. After an examination of a wide variety of references, Wiscombe and Warren (1980) concluded that the average grain radii are in the range 20–100 μm for new snow; 100–300 μm for fine-grained older snow; and 1000–1500 μm for old snow near the melting point. The selection of snow grain size and other variables are subject to environmental conditions.

Optical properties of pure snow/ice and soot contamination were obtained for the present study through Mie computations (Wiscombe and Warren 1980; Warren and Wiscombe 1980). Since absorption of pure snow/ice predicted by Mie computations is negligible in the visible, Warren and Wiscombe (1980) introduced trace amounts of absorptive impurities such as graphitic soot to match observed snow albedo. This alters the snow/ice albedo only in the visible, and changes nothing for the rest of the spectral wavelengths because of the high imaginary refractive index for ice throughout the infrared region.

Observations show that the mass-fraction (f) of soot ranges from 0.01 to 0.06 ppmw (parts per million by weight) in arctic snow/ice (Warren 1982). For a mixture of snow/ice and impurities, the optical properties of the mixture are obtained by weighting each component properly. Thus, β_{ext} , ω and g of the mixture are obtained as follows:

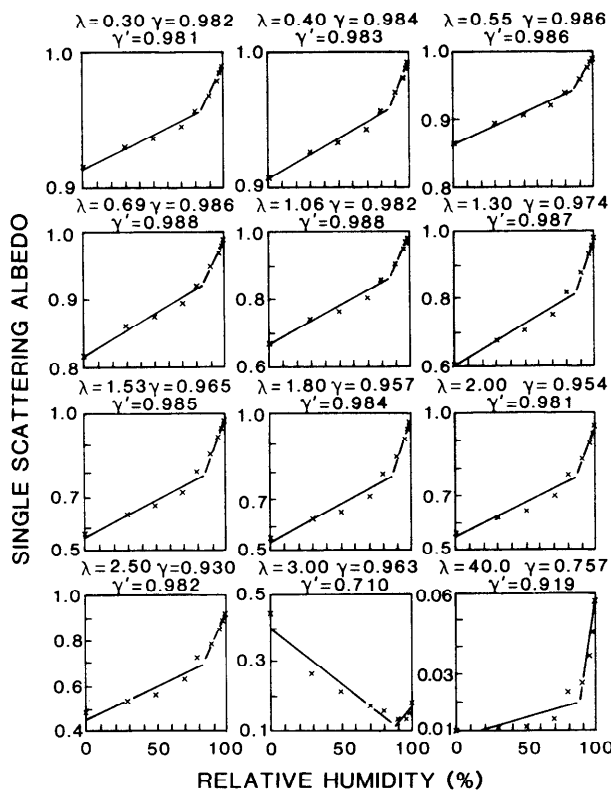


FIG. 9. Least squares fits of single scattering albedo form wavelength 0.3 to 40 μm for arctic haze model (γ denotes correlation coefficient for dry condition and γ' for wet condition).

$$\beta_{\text{ext}}(\text{RG}) = \rho(\text{RG})[(1-f)k_{\text{ext}}(\text{ice}) + fk_{\text{ext}}(\text{soot})]$$

$$\omega(\text{RG}) = \frac{(1-f)k_{\text{sca}}(\text{ice}) + fk_{\text{sca}}(\text{soot})}{(1-f)k_{\text{ext}}(\text{ice}) + fk_{\text{ext}}(\text{soot})}$$

$$g(\text{RG}) = \frac{(1-f)k_{\text{sca}}(\text{ice})g(\text{ice}) + fk_{\text{sca}}(\text{soot})g(\text{soot})}{(1-f)k_{\text{sca}}(\text{ice}) + fk_{\text{sca}}(\text{soot})} \quad (12)$$

where k_{ext} and k_{sca} are the mass extinction and scattering cross sections for each component, respectively; $\rho(\text{RG})$ is the density of the mixture for each grain radius and can be approximated by the density of snow/ice only, due to the relatively small amounts of soot present.

3. Analysis of the Arctic Stratus Cloud Experiment

a. Comparison

Broadband measurements of solar and terrestrial radiation in the Arctic Stratus Cloud Experiment of 1980 were reported by Herman and Curry (1984) and Curry and Herman (1985), respectively. The physical properties of the arctic stratus, together with the associated meteorological conditions, were reported by Tsay and Jayaweera (1984). No arctic haze measurements were made concurrently. Figure 10 shows two atmospheric profiles for the low stratus clouds, which are used for model comparison and sensitivity studies. Two-layer clouds associated with the surface and cloud top inversions were observed on 28 June 1980. A single-layer

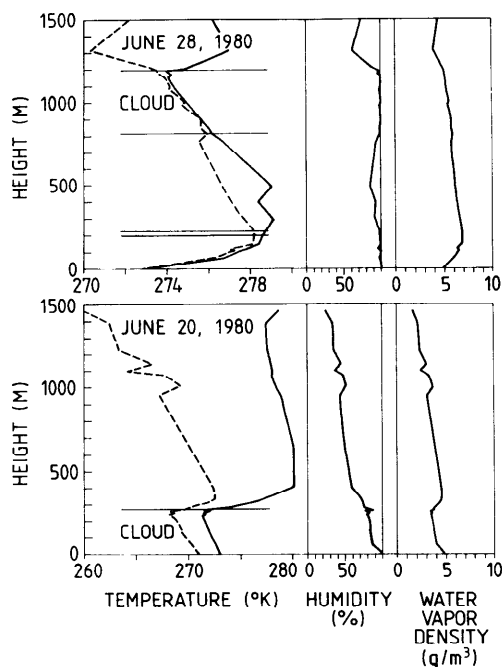


FIG. 10. Atmospheric profiles for two observed arctic stratus clouds on June 20 and 28, 1980 (dashed: for dew point temperature).

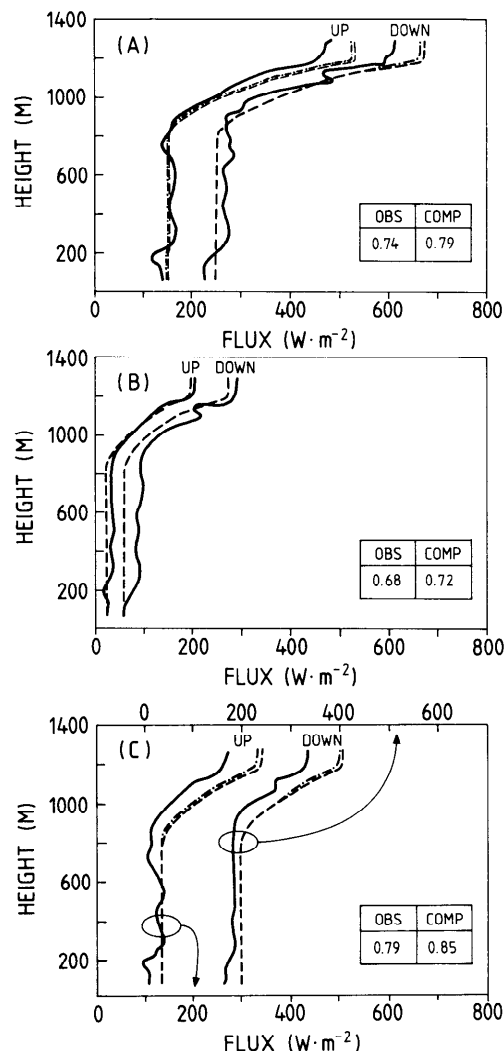


FIG. 11. Comparison of observed (solid) and computed fluxes for stratus clouds on 28 June 1980; (a) for total flux, (b) for near-IR, (c) for visible, and values in inset for albedo at cloud top. (dashed) for fluxes computed from cloud model only and (dot-dashed) from model with both cloud and haze; but these two curves can not be distinguished in (b).

cloud was measured on 20 June 1980. This single-layer cloud extended to the surface and was capped by a strong inversion at the cloud top. The clouds observed on both days were not saturated; they showed a relative humidity range from as low as about 80% on 20 June. In general, dry conditions were observed above the clouds.

We have computed radiative fluxes for the solar spectrum (0.28–4.0 μm), the near-infrared (NIR, 0.78–4.0 μm), and the visible (VIS, 0.28–0.78 μm), corresponding to the sensitivity ranges of the Eppley pyranometers. Boundary conditions were taken from the observed data. They are 53.8° (28 June) and 53.6° (20 June) for solar zenith angles; and 0.68 (VIS, 28 June), 0.35 (NIR, 28 June), 0.60 (VIS, 20 June) and 0.43

(NIR, 20 June) for surface albedos. The solar constant ($0.28\text{--}4.0\ \mu\text{m}$) was taken to be $1337.19\ \text{W m}^{-2}$. Model comparisons should include not only bulk quantities, such as reflectivity, transmissivity and absorptivity which are relative ratios, but also flux and heating/cooling profiles. The computed bulk radiative quantities have been reported in good agreement with the measurements (Herman and Curry 1984); we present here the comparison of flux profiles. Figures 11 and 12 show the computed (dashed and dot-dashed lines) and observed (solid lines) upward and downward fluxes on 28 June and 20 June, respectively. The measured fluxes for the visible region are obtained as the difference between the total and the near-infrared (Herman and Curry 1984).

Generally, the agreement between computed (based upon measured cloud microphysics and broad-band surface albedo) and observed fluxes is fair. The major discrepancy occurs at the cloud top, where the fluxes differ by up to about $70\ \text{W m}^{-2}$. There was some difference in flux measurement between the Eppley and silicon detectors, which should not be fully responsible for this discrepancy. For instance, an instrumental difference among detectors of about 2% and 10% in total transmissivity and reflectivity (pp. 14 and 15 of Herman and Curry 1984) corresponds to about 15 and $50\ \text{W m}^{-2}$ in downward and upward fluxes, respectively. In addition to the uncertainty in the measurements, three causes may be responsible for the discrepancies between observed and computed fluxes. They are (1) the improper use of spectrally fixed surface albedo in the model, (2) the insufficient absorption of clouds in the visible region, and (3) the improperly determined cloud top geometry.

b. Discussion

To investigate the adequacy of using a fixed surface albedo in the model, the spectral snow albedos were obtained from repeated computations by changing surface conditions to match the observed broadband snow albedos in the visible and near-infrared. The use of fixed albedo overestimates fluxes in $0.3\text{--}0.6\ \mu\text{m}$ region and underestimates fluxes in $0.7\text{--}1.0\ \mu\text{m}$ region. These regions are associated with the major solar energy and the weak gaseous and droplet absorptions, respectively. The use of spectral rather than fixed snow albedo reduces the discrepancy between observed and computed fluxes by about 3 to $5\ \text{W m}^{-2}$.

Since the early 1950s, a cloud absorptivity paradox has been noted (Fritz 1951). The absorption of clouds predicted by theoretical calculations at 6%, is far less than the actually measured values of about 20% absorption. Subsequent aircraft measurements (e.g., Reynolds et al. 1975) obtained even larger cloud absorption than before—about 20–40%. This discrepancy was recently attributed to the leakage of radiation through cloud sides (Welch et al. 1980), the effects

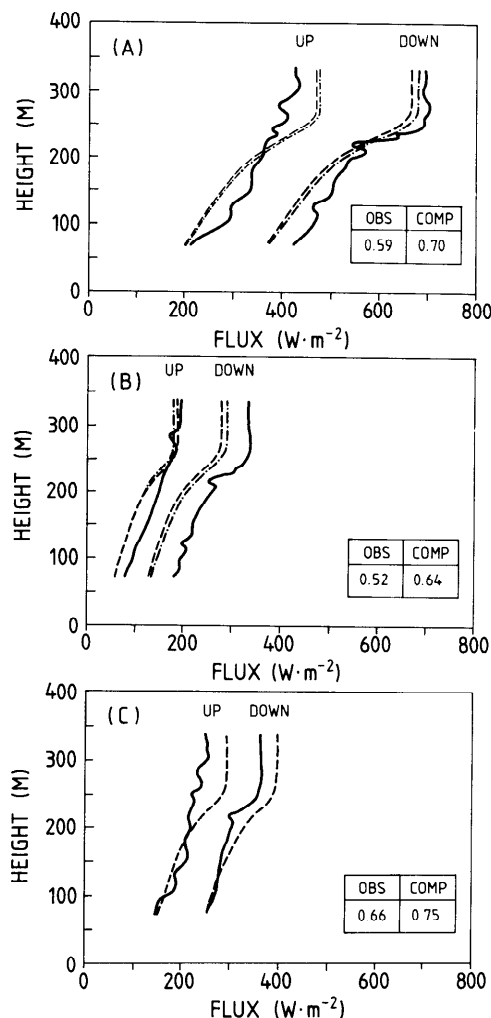


FIG. 12. As in Fig. 11, except for 20 June 1980: (dashed) for fluxes computed from cloud model only and (dot-dashed) from cloud model with water vapor reduced to half; but these two curves can not be distinguished in (c).

of very large droplets (Wiscombe et al. 1984), or the effects of graphitic carbon (Chýlek et al. 1984). However, the first two explanations are not applicable to the problem of arctic stratus. The leakage of radiation through cloud sides is important for cumulus clouds (which may be modeled approximately by cubes) but is probably negligible for extended stratiform clouds. Cloud absorption is increased by about 2% to 4% due to very large drops in the $40\text{--}50\ \mu\text{m}$ radius range, which allow solar radiation to penetrate deeply into the clouds. But such large drops were not observed during the Arctic Stratus Cloud Experiment; drop radii of about $20\text{--}25\ \mu\text{m}$ were the maximum. Therefore, we are left with the possibility that cloud impurities may play an important role in increasing cloud absorption. Indeed, there is plenty of soot in the arctic atmosphere (Shaw 1982). Curves marked with dot-

dashed in Fig. 11 are computed for a hazy sky condition, corresponding to an optical depth of about 0.06 at $0.5 \mu\text{m}$ wavelength in the arctic summer (Shaw 1982). The haze lead to some reduction of fluxes in the visible but not in the near-infrared regions. Better agreement in the near-infrared was obtained by reducing the water vapor density by 50% for the entire column on 20 June instead of introducing haze. But 50% errors in water vapor density correspond to 10% (or 30°K) errors in dewpoint temperature measurements, which seems an unlikely explanation for the discrepancy between the observed and computed downward flux (NIR) on June 20.

In the plane-parallel approximation, boundary layers of cloud-air interface are assumed to be horizontally homogeneous, and this assumption differs somewhat with the observed wavy cloud top geometry (Tsai and Jayaweera 1984). A different radiation field is expected for this wavy condition. The downward fluxes at the cloud top and base were determined from the average fluxes measured within a 100 m layer above and below the cloud layer, respectively (p. 9 of Herman and Curry 1984). Also, the upward flux at cloud top was estimated by extrapolating the upward fluxes within the cloud layer to the cloud top, due to the wavy geometry at the cloud top. This introduces additional uncertainties in the flux measurements. Recent theoretical studies of radiation fields in horizontally inhomogeneous media (e.g., Stephens 1986) found that the reflectance (or upward flux) is lower for both absorbing and non-absorbing media. More careful studies of the cloud top geometry effect are needed.

Unfortunately, corresponding measurements of infrared fluxes in the atmospheric profiles for 20 and 28 June were not reported in the paper of Curry and Herman (1985). Only four out of twelve profiles in the paper of Herman and Curry (1984) were documented and two of them were altostratus clouds. Thus, the following theoretical studies in the infrared region can not be compared with measurements.

4. Sensitivity studies

a. Surface conditions

To study the energy budget of both solar and terrestrial radiation, the surface condition has to be properly simulated. In the arctic summer the surface conditions are generally very complicated. Thus, the surface may be composed of open leads, pack ice, melting ponds, refrozen ice, old snow, new snow, etc. From the flight notes and pictures, the surface on 28 June (at 77°N) is known to be essentially snow covered. Visual data for 20 June were not available since the cloud extended to the surface. Broadband surface albedos, such as total, visible and near-infrared are often measured instead of detailed spectral albedos.

The variability of the spectral albedo for snow is illustrated in Fig. 13, which shows computed snow al-

bedo as a function of grain radius, density, impurity and atmospheric conditions. New snow generally has a higher spectral albedo than old snow. The larger snow grains of older snow tend to produce further absorption, due to the deeper penetration of the photons. Generally, snow grains increase in size with depth, but the snow density is not related to grain size and ranges from about 0.15 to 0.5 g cm^{-3} . For instance, wind-packed snow in the Arctic often has a small grain radius of about $100 \mu\text{m}$ but a high density of about 0.45 g cm^{-3} . Therefore, wind-packed snow has an even higher spectral albedo than new snow. Under such conditions, photons are efficiently backscattered in the upper layer and only a small portion of the radiation will reach the large grains below and be absorbed. Thus, the spectral albedo of snow depends sensitively upon the environmental conditions.

To simulate the surface condition of 28 June, the grain radius is assumed to be $2000 \mu\text{m}$, corresponding to snow near the melting point. The mass-fraction of soot in the snow is adopted to be 0.24 ppmw , which may be somewhat larger than the observed value. However, it leads to computed broadband albedo values matching closely the observed broadband albedo of the total (0.57), visible (0.68) and near-infrared (0.35) regions. Therefore, we use this surface condition to investigate the effects of various atmospheric conditions on the radiation budget.

b. Solar radiation

Figure 14 shows the atmospheric heating profiles under various conditions. The base line is represented by "CLOUD" only. The exclusion of CO_2 and O_2 ab-

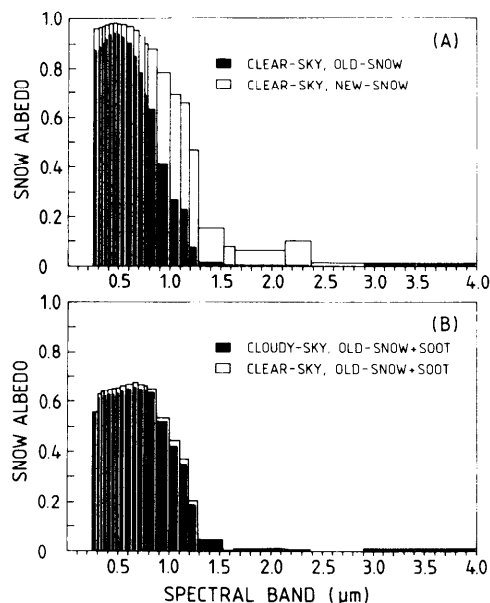


FIG. 13. Spectral albedo of snow as function of grain size (old-snow and new-snow), impurity (soot) and sky condition.

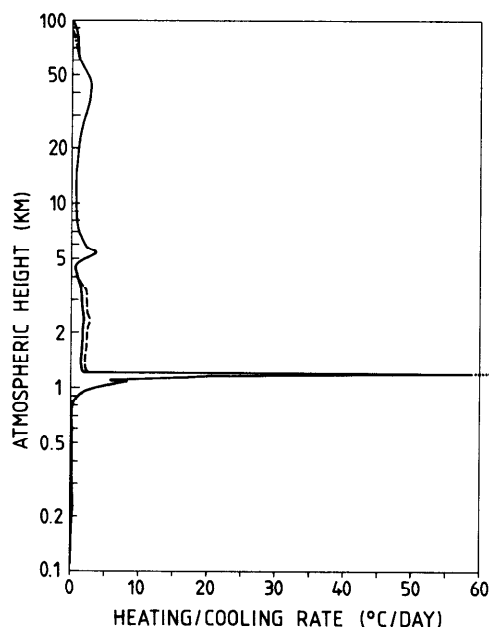


FIG. 14. Atmospheric heating profiles for various conditions on 28 June 1980 (solid: CLOUD, dashed: CLOUD + HAZE(A), dotted: CLOUD-CO₂-O₂; CLOUD + HAZE(B) and HAZE(C) overlapped with CLOUD and can not be seen in this figure).

sorption is denoted by "CLOUD - CO₂ - O₂." "HAZE(A)" and "HAZE(C)" denote the condition of dry haze, located above the upper cloud and between the upper and lower clouds, respectively. "HAZE(B)" is the wet haze condition, for which the haze is imbedded in the cloud and mixed with the drops for the entire cloud. The optical depth of all haze layers is adopted to have the value of 0.06 at 0.5 μm wavelength, implying that the geometrical thickness of haze layers may be different.

Strong cloud heating takes place in the upper 100 m and reaches about $60^\circ\text{C day}^{-1}$ (or 5°C h^{-1}). This heating profile corresponds to local solar noon. Because of the relatively drier and colder air aloft in the Arctic than elsewhere, more radiation reaches the cloud and is available for cloud drop absorption. A similar enhancement is found when the absorption of CO₂ and O₂ is excluded, resulting in extra heating in the upper part of the cloud. The inclusion of haze layers does not alter the atmospheric heating significantly, except for a $0.7^\circ\text{C day}^{-1}$ increase when HAZE(A) is introduced above the cloud from 1.2 to 3.8 km height. Spectral absorption of the clouds for dry and wet haze conditions are shown in Fig. 15. The white areas between the two curves of net fluxes at boundaries represent the flux divergence. Dry haze particles absorb strongly at visible wavelengths while drops do not. In the near-infrared, the opposite situation is found, except for the 0.9 and 1.3 μm bands. When haze particles absorb water vapor (wet haze condition), they start losing their identities and behave like tiny droplets. However, the

absorption bands of wet haze overlap completely with those of the cloud absorption. Thus, with the assumption of external mixing, implying that the haze particles occur in the interstitial areas between drops but not inside the drops themselves, the absorption of wet haze particles is strongly diluted by cloud absorption [e.g. Eq. (10)]. When haze exists between the clouds [HAZE(C)] with high relative humidity (RH > 80%, Fig. 10), little radiation is absorbed by the haze. This is because the strong scattering in the visible and strong absorption in the near-infrared by the upper cloud leaves little radiation to interact with the haze. The finding of aerosols increasing absorption in clouds by about 1% to 5% by Herman and Curry (1984) is due to their neglect of the humidity effect in their adopted haze model of Shettle and Fenn (1976).

Tables 1 and 2 show fluxes computed for solar and near-infrared radiation with various atmospheric conditions on 28 and 20 June. The "CLEAR" case is made by artificial removal of the cloud. The exclusion of

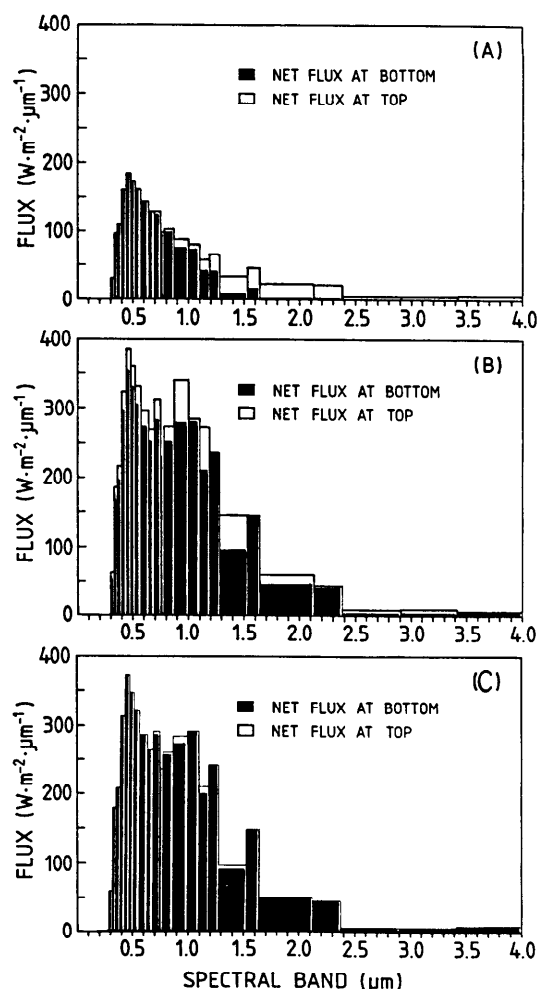


FIG. 15. Spectral absorption of (a) cloud, (b) dry haze and (c) wet haze models.

TABLE 1. Model computations of fluxes for solar and near-infrared (in parentheses) radiation with various components in the atmospheric profile of 28 June 1980 ($F^+(0)$ denotes upward flux at top; $F^-(\tau_N)$, downward flux at bottom; ΔF_{sfic} , net flux gain at surface; ΔF_{atm} , net flux gain of entire atmosphere; ΔF_{lyr} , net flux at haze layer [all in dimension of W m^{-2}]). Solar zenith angle is 53.8° yielding input solar flux at top of 789.76 W m^{-2} and near-infrared flux at top of 360.20 W m^{-2} .

Components	$F^+(0)$	$F^-(\tau_N)$	ΔF_{sfic}	ΔF_{atm}	ΔF_{lyr}
Cloud	517.00 (187.82)	242.77 (57.79)	101.20 (37.74)	171.56 (134.64)	38.47* (38.02)*
Cloud-CO ₂ -O ₂	521.86 (189.58)	244.39 (57.94)	101.91 (37.88)	165.98 (132.74)	39.55* (39.23)*
Cloud + Haze (A)	503.37 (184.73)	237.33 (57.14)	99.16 (37.34)	187.23 (138.14)	16.31 (3.73)
Cloud + Haze (B)	517.00 (187.82)	242.77 (57.79)	101.20 (37.74)	171.56 (134.64)	0.00 (0.00)
Cloud + Haze (C)	516.72 (187.81)	241.03 (57.61)	100.59 (37.64)	172.45 (134.76)	0.90 (0.12)
Clear	333.10 (65.21)	647.07 (259.45)	319.18 (192.91)	137.47 (102.09)	— —
Clear-CO ₂ -O ₂	335.60 (65.23)	652.93 (262.16)	322.99 (195.59)	131.16 (99.38)	— —
Clear + Haze (A)	326.62 (64.71)	635.93 (257.13)	314.40 (191.20)	148.74 (104.29)	11.65 (2.33)

* Net flux gain at cloud layer.

CO₂ and O₂ increases surface absorption by 0.7 W m^{-2} in the cloudy case and 3.8 W m^{-2} in the clear case (Table 1). This increase is mainly caused by the lacking absorption of radiation by O₂ in the $0.7 \mu\text{m}$ band. Also, the entire atmosphere loses about 6 W m^{-2} and the additional heating in the cloud top (Fig. 14) is caused by extra absorption of 1 W m^{-2} due to lack of CO₂. The introduction of HAZE(A) into the cloudy atmosphere decreases the surface absorption by about $2\text{--}3 \text{ W m}^{-2}$, because soot-contaminated snow has absorption bands similar to the dry haze in the visible region. This effect is enhanced (about 5 W m^{-2}) when the haze is added to a clear atmosphere, due to larger amounts of radiation available. The increase in at-

mospheric absorption due to HAZE(A) ranges from 11 to 17 W m^{-2} for clear and cloudy conditions, respectively. Eighty percent of this absorption comes from visible wavelengths, as expected. However, the absorption of HAZE(A) reduces the absorption of the underlying cloud by about 1 W m^{-2} . Indeed, a dry haze particle is a relatively efficient absorber, implying that the flux absorbed by the haze is 30%–40% of that absorbed by the cloud, despite its small optical depth.

c. Terrestrial radiation

The solar heating of the earth-atmosphere system has to be balanced by the infrared cooling. In the infrared region, pure snow and soot-contaminated snow

TABLE 2. As in Table 1, except for 20 June 1980 and input solar flux at top of 793.52 W m^{-2} ; near-infrared flux at top of 361.92 W m^{-2} for 53.6° zenith angle.

Components	$F^+(0)$	$F^-(\tau_N)$	ΔF_{sfic}	ΔF_{atm}	ΔF_{lyr}
Cloud	492.77 (176.86)	353.88 (109.92)	151.31 (62.91)	149.44 (122.15)	31.23* (30.90)*
Cloud-CO ₂ -O ₂	497.64 (178.67)	356.31 (110.40)	154.45 (63.39)	143.43 (119.85)	32.19* (31.94)*
Cloud + Haze (A)	480.22 (174.00)	346.05 (108.67)	143.27 (62.28)	165.03 (125.64)	13.01 (2.98)
Cloud + Haze (A and B)	491.00 (176.46)	352.78 (109.75)	150.88 (62.83)	151.64 (122.63)	2.06 (0.45)
Clear	364.33 (93.77)	669.02 (275.04)	313.80 (178.92)	115.39 (89.23)	— —
Clear + Haze (A)	357.41 (92.62)	657.82 (272.87)	309.08 (177.54)	127.03 (91.76)	11.86 (2.57)

have relatively simple characteristics. The emissivity of snow is quite insensitive to the snowpack parameters (i.e., grain size, density) and can be approximated to be 0.99 as measured by Griggs (1968). Table 3 shows infrared fluxes computed for 20 and 28 June, under various atmospheric conditions. The effect of HAZE(A) on the thermal radiation is less than 1 W m^{-2} under both cloudy and clear conditions. Under clear skies, the downward flux at the surface for 28 June is 25 W m^{-2} larger than that of 20 June. The surface inversion on 28 June is responsible for this, and also the water vapor density is very high, which makes absorption saturate easily. The net loss from the surface is due to radiation escaping in the window region. However, when clouds are present, the return radiation from the cloud to the surface offsets the cooling greatly. This results in a net warming at the surface for 28 June. Since clouds are very efficient emitters, intensive cooling is found in the upper 100 m. The upper cloud on June 28 is much denser than on June 20; therefore, stronger cooling is expected. The low-level cloud on June 28 is very thin and underlies a dense cloud, which prevents its further cooling.

d. Net radiation budget and inferred melting rates

After examining the solar and terrestrial radiative components in the Arctic, it would be interesting to see the net effects. Doing this involves tremendous computations, assumptions and uncertainties. For instance, the radiation field is strongly dependent on the atmospheric temperature and composition, such as clouds, haze particles, etc. Changes of the radiation forcing will lead to dynamical mixing internally. Subsequently, the changes in atmospheric temperature and composition feed back into the radiation field. These events take place under the assumed absence of external forcings, such as advection. All these processes may occur simultaneously, however, and they remain poorly understood. In spite of this circumstance, it may still be worthwhile to isolate some processes to get a basic understanding of others.

TABLE 3. Model computations of fluxes for infrared radiation with various components in atmospheric profiles of 20 and 28 June 1980 (notations as in Table 1, except $F^+(\tau_N)$ for upward flux at surface).

Components	$F^+(\tau_N)$	$F^-(\tau_N)$	ΔF_{atm}	$F^+(0)$	ΔF_{atm}
(a) 20 June 1980 (single-layer cloud)					
Clear	313.83	232.28	-81.55	253.60	-172.05
Haze (A)	313.84	232.78	-81.06	253.61	-172.55
Cloud + Haze (A)	314.65	313.72	-0.93	249.46	-248.53
(b) 28 June 1980 (multi-layer clouds)					
Clear	314.09	257.65	-56.44	247.99	-191.55
Cloud	314.78	327.53	+12.75	246.16	-258.91
Cloud + Haze (A)	314.78	327.53	+12.75	246.19	-258.94

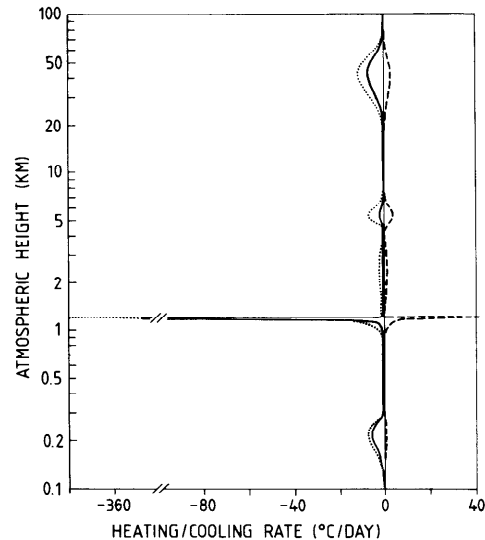


FIG. 16. Daily solar heating and infrared cooling profiles for cloudy condition on 28 June 1980: (dashed) for solar, (dotted) for infrared, and (solid) for net radiation.

The persistent characteristics of the arctic stratus clouds and haze particles suggest that their mean conditions may not change dramatically with time. Therefore, the integration of the radiation field over a short period of time may be justified. Solar radiation is highly dependent on zenith angle. However, under the assumption of a steady atmospheric composition, the infrared radiation remains time independent. Figures 16 and 17 show a 24-hour integration of solar heating and infrared cooling, together with the net effects, for the cloudy conditions of 28 and 20 June. Very intense net cooling is achieved near the cloud top on 28 June. The solar heating for 24 hours integration is reduced by about 20% compared to the computed value for local solar noon (Fig. 14). Intense mixing between the cloud layer and entrained air is expected to result from this strong cooling. However, the low-level cloud undergoes a net cooling, which indicates that in this particular case the lower-level cloud will not dissipate due to radiation. On 20 June, a slightly different picture is found. The net cooling at the cloud top is only about one-third of that on 28 June. A slight heating is also found at about 100 m below the cloud top. For this less dense and low-level cloud, the solar radiation may penetrate into the cloud layer but the infrared cooling is not enough to offset it, resulting in a net heating. This effect has been used to explain the layering of arctic stratus cloud by Herman and Goody (1976).

Table 4 shows the fluxes integrated for 24 hours with various atmospheric conditions on 20 and 28 June. In the clear condition on 20 June, the HAZE(A) reduces the downward flux at the surface by about 12 W m^{-2} , which is about 16 times less than the reduction due to the cloud. However, it is still efficient enough to offset a warming due to a potential doubling of the CO_2

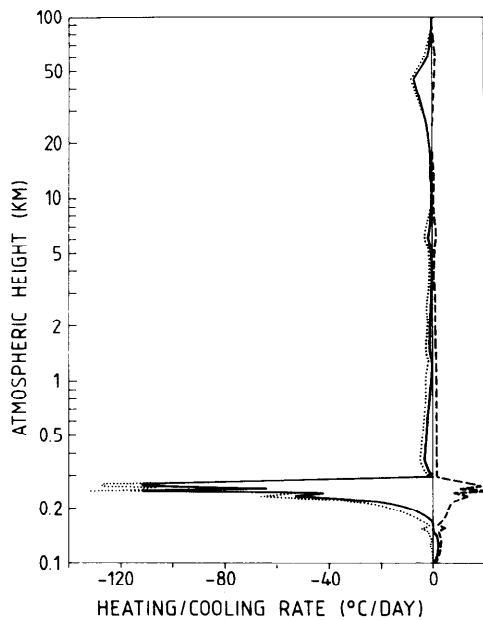


FIG. 17. As in Fig. 16, except for 20 June 1980.

amount, which increases the downward flux at the surface by about 4 to 7 W m^{-2} (Tsay 1986). Multiple scattering enhances the absorption of HAZE (A) in the layer, but the location of the haze layer is more important. On 28 June (cloud top at 1.2 km), a net absorption of 14 W m^{-2} is found in the haze layer, but it is only 4 W m^{-2} for 20 June (cloud top at 0.3 km), due to more competition with gaseous absorption.

The absorption of the snow surface is larger under a clear sky than under a cloudy sky in late June. In the case of 20 June, a total amount of 104 W m^{-2} is absorbed under a clear sky, but only 84 W m^{-2} under a cloudy sky. On June 28, this difference is even further enhanced to 132 W m^{-2} under a clear sky and 70 W m^{-2} under a cloudy sky. These results support the early finding of Vowinkel and Orvig (1970). The absorption of 1 W m^{-2} corresponds to a melting rate of ice at about 0.84 cm month^{-1} , or 2.36 cm month^{-1} for snow. As can be expected, if the snow/ice starts to melt this process will be accelerated, due to the decrease in surface albedo (Wiscombe and Warren 1980).

5. Summary and conclusion

A comprehensive radiation model has been constructed which includes scattering and absorption/emission by molecules, as well as by cloud droplets, haze particles and surface snow grains. Mie scattering properties for drops are parameterized as functions of the second and third moments of the drop size distributions throughout the solar and terrestrial spectra. Good fits of these optical properties for stratiform clouds are obtained. For Arctic haze and snow conditions, the optical properties computed by Blanchet

and List (1983) and Warren and Wiscombe (1980) are adopted, respectively. Thus, a unified treatment of shortwave and longwave radiative transfer is achieved. Relative humidity effects of the haze particles are also considered. Snow conditions of the arctic region are simulated by snow grain size and soot contamination in the surface layers. External mixing is employed for cloud droplets with haze particles and for pure snow/ice with graphitic soot.

Data collected during the Arctic Stratus Cloud Experiment in 1980 are used for model comparisons and sensitivity studies under cloudy and hazy sky conditions. Model computed bulk radiative quantities are generally in good agreement with measurements, since they are ratios of fluxes and are not sensitive to changes in absolute values. The large discrepancy between measured and computed fluxes at the cloud top may arise from experimental uncertainties and the data reduction procedure as well as the improper treatment of cloud top geometry in the model. Investigations of this discrepancy aimed at gaining a better understanding of the climate in the Arctic, require advanced experiments such as FIRE (Cox et al. 1987) emphasizing the cloud-air interface. Such experiments are urgently needed. Meanwhile, fast and accurate radiative transfer models must be developed in which both the geometry effect in multiple scattering and the molecular absorption are taken into account.

Sensitivity studies are conducted for the conditions of arctic summer, during which the arctic stratus clouds

TABLE 4. Model computations of fluxes in daily radiation with various components in atmospheric profiles of 20 and 28 June 1980 (notations as in Table 1, except (S) for solar and (I) for infrared radiation).

Components	$F^-(\tau_N)$	ΔF_{atm}	$F^+(0)$	ΔF_{atm}	ΔF_{lyr}
<i>(a) 20 June 1980 (single-layer cloud)</i>					
Clear (S)	418.18	+185.12	249.73	75.97	—
Clear (I)	232.28	-81.55	253.60	-172.05	—
Haze (A) [S]	406.20	+181.75	244.30	84.77	+8.97
Haze (A) [I]	232.78	-81.06	253.61	-172.55	-0.53
Cloud (S)	197.15	+84.30	321.87	104.65	+9.94
+ Haze (A)					+5.52
Cloud (I)	313.72	-0.93	249.46	-248.53	-74.24
+ Haze (A)					-1.76
<i>(b) 28 June 1980 (multi-layer clouds)</i>					
Clear (S)	407.06	+188.24	232.94	+93.94	—
Clear (I)	257.65	-56.44	247.99	-191.55	—
Cloud (S)	136.04	+56.65	346.94	+111.53	+18.15
Cloud (I)	327.53	+12.75	246.16	-258.91	-79.50
Cloud (S)	132.45	+55.30	336.57	+123.24	+17.98
+ Haze (A)					+16.48
Cloud (I)	327.53	+12.75	246.19	-258.94	-77.54
+ Haze (A)					-2.62

are a persistent feature. Intensive solar heating and infrared cooling occur in the upper 100 m of the cloud layer. The presence of clouds decrease the downward flux at the surface by about $130\text{--}200\text{ W m}^{-2}$. This is inferred by artificially removing the stratus clouds from two observed profiles. Arctic haze in the summertime is important if it is located above the cloud layer or in air with low relative humidity. It also decreases the downward flux at the surface, but only by about $10\text{--}12\text{ W m}^{-2}$. By comparison the greenhouse effect of doubling the CO_2 amount increases the downward flux at the surface by about $4\text{--}7\text{ W m}^{-2}$ (Tsay 1986) in the clear McClatchey atmospheres and can be offset by the background haze (dry condition) or by an increase in cloudiness of about 4%.

Assuming steady microstructures of stratus clouds in late June, we find that a clear sky condition results in more available downward flux ($100\text{--}130\text{ W m}^{-2}$) for snow melt (9.3 cm day^{-1}) than does a cloudy sky condition ($70\text{--}80\text{ W m}^{-2}$ or 6 cm day^{-1}). This is because the increase of infrared radiation diffused back to the surface by the cloud can not compensate for the reduction of solar radiation. When the snow starts to melt, the decreasing snow albedo further accelerates the melting process.

Acknowledgments. We are very pleased to acknowledge Drs. A. Slingo, S. Warren and W. Wiscombe for providing their data sets. One of us (SCT) greatly appreciates the continued encouragement and support of this work by Dr. G. Stephens. This study was supported by the National Science Foundation through Grant DPP 84-06093.

REFERENCES

- Blanchet, J., and R. List, 1983: Estimation of optical properties of arctic haze using a numerical model. *Atmos.-Ocean*, **21**, 444–465.
- Carlson, T. N., 1981: Speculations on the movement of polluted air to the Arctic. *Atmos. Environ.*, **17**, 1473–1477.
- Carrier, L. W., G. A. Cato and K. J. von Essen, 1967: The back-scattering and extinction of visible and infrared radiation by selected major cloud models. *Appl. Opt.*, **6**, 1209–1216.
- Chandrasekhar, S., 1960: *Radiative Transfer*, Dover, 393 pp.
- Chou, M. D., and A. Arking, 1980: Computation of infrared cooling rates in the water vapor bands. *J. Atmos. Sci.*, **37**, 855–867.
- , and —, 1981: An efficient method for computing the absorption of solar radiation by water vapor. *J. Atmos. Sci.*, **38**, 798–807.
- Chýlek, P., V. Ramaswamy and R. J. Cheng, 1984: Effect of graphitic carbon on the albedo of clouds. *J. Atmos. Sci.*, **41**, 3076–3084.
- Coulson, K. L., 1975: *Solar and Terrestrial Radiation: Methods and Measurements*. Academic Press, 322 pp.
- Cox, S. K., D. S. McDougal, D. A. Randall and R. A. Schiffer, 1987: FIRE—the First ISCCP Regional Experiment. *Bull. Amer. Meteor. Soc.*, **68**, 114–118.
- Curry, J. A., and G. F. Herman, 1985: Infrared radiative properties of summertime arctic stratus clouds. *J. Climate Appl. Meteor.*, **24**, 525–538.
- Feigelson, E. M., 1964: *Light and Heat Radiation in Stratus Clouds*. Academy of Sciences, Moscow, 245 pp.
- Fritz, S., 1951: Solar radiant energy. *Compendium of Meteorology*, T. F. Malone, Ed., Wiley, 14–29.
- Griggs, M., 1968: Emissivities of natural surfaces in the 8- to 14-micron spectral region. *J. Geophys. Res.*, **73**, 7545–7551.
- Hansen, J. E., and J. B. Travis, 1974: Light scattering in planetary atmospheres. *Space Sci. Rev.*, **16**, 527–610.
- Herman, G. F., 1977: Solar radiation in summertime arctic stratus clouds. *J. Atmos. Sci.*, **34**, 1423–1432.
- , and R. Goody, 1976: Formation and persistence of summertime arctic stratus clouds. *J. Atmos. Sci.*, **33**, 1537–1553.
- , and J. A. Curry, 1984: Observational and theoretical studies of solar radiation in arctic stratus clouds. *J. Climate Appl. Meteor.*, **23**, 5–24.
- Huschke, R. E., 1969: Arctic cloud statistics from air calibrated surface weather observations. Mem. RM-6173-PR, Rand Corp., Santa Monica, CA, 79 pp.
- Jayaweera, K., and T. Ohtake, 1973: Concentration of ice crystals in arctic stratus clouds. *J. Rech. Atmos.*, **7**, 199–207.
- Kellogg, W. W., 1975: Climatic feedback mechanisms involving the polar regions. *Climate of the Arctic*, G. Weller and S. Bowling, Eds., University of Alaska Press, 436 pp.
- Kneizys, F. X., E. P. Shettle, W. O. Gallery, J. H. Chetwynd, Jr., L. W. Abreu, J. E. A. Selby, R. W. Fenn and R. A. McClatchey, 1980: Atmospheric transmittance/radiance: Computer code LOWTRAN 5. Air Force Geophysics Lab, AFGL-TR-80-0067, 233 pp.
- Liou, K. N., 1980: *An Introduction to Atmospheric Radiation*, Academic Press, pp 392.
- McClatchey, R. A., W. S. Benedict, S. A. Clough, D. E. Burch, R. F. Calfee, K. Fox, L. S. Rothman and J. S. Garing, 1973: AFCRL atmospheric absorption line parameters compilation. Air Force Cambridge Research Laboratories, AFCRL-TR-73-0096, 78 pp.
- Mugnai, A., and W. J. Wiscombe, 1980: Scattering of radiation by moderately nonspherical particles. *J. Atmos. Sci.*, **37**, 1291–1307.
- Patterson, E. M., B. T. Marshall, and K. A. Rahn, 1982: Radiative properties of the arctic aerosol. *Atmos. Environ.*, **16**, 2967–2977.
- Penndorf, R., 1957: Tables of the refractive index for standard air and the Rayleigh scattering coefficient for the spectral region between 0.2 and $20\text{ }\mu\text{m}$ and their application to atmospheric optics. *J. Opt. Soc. Am.*, **47**, 176–182.
- Reynolds, D., T. Vonder Haar and S. Cox, 1975: The effect of solar radiation absorption in the tropical atmosphere. *J. Appl. Meteor.*, **14**, 433–444.
- Rothman, L., 1981: AFGL atmospheric absorption line parameters compilation: 1980 version. *Appl. Opt.*, **20**, 791–795.
- Shaw, G., 1982: Atmospheric turbidity in the polar regions. *J. Appl. Meteor.*, **21**, 1080–1088.
- , 1985: On the climatic relevancy of arctic haze: Static energy balance considerations. *Tellus*, **37**, 50–52.
- Shettle, E. P., and R. W. Fenn, 1976: Models for the atmospheric aerosol and their optical properties. *Proc. AGARD Conf. (183) Optical Propagation in the Atmosphere*, Lyngby, Denmark, 245 pp.
- , and —, 1979: Models for the aerosols of the lower atmosphere and the effects of humidity variations on their optical properties. Rep. No. AFGL-TR-0214, Hanscom AFB, Ma., 94 pp.
- Slingo, A., and H. M. Schrecker, 1982: On the shortwave radiative properties of stratiform water clouds. *Quart. J. Roy. Meteor. Soc.*, **108**, 407–426.
- Stamnes, K., 1986: The theory of multiple scattering of radiation in plane parallel atmospheres. *Rev. Geophys.*, **24**, 299–309.
- , S. C. Tsay, W. Wiscombe and K. Jayaweera, 1988: Numerically stable algorithm for discrete-ordinate-method radiative transfer in multiple scattering and emitting layered media. *Appl. Opt.*, **27**, 2502–2509.
- Stephens, G. L., 1978: Radiation profiles in extended water clouds. I: Theory. *J. Atmos. Sci.*, **35**, 2111–2122.
- , 1979: Optical properties of eight water cloud types. CSIRO Aust. Div. Atmos. Phys. Tech. Pap. No. 36, 35 pp.
- , 1984: The parameterization of radiation for numerical weather prediction and climate models. *Mon. Wea. Rev.*, **112**, 826–867.

- , 1986: Radiative transfer in spatially heterogeneous, two-dimensional, anisotropically scattering media. *J. Quant. Spectrosc. Radiat. Transfer*, **36**, 51–67.
- Tsay, S. C., 1986: Numerical study of the atmospheric radiative transfer process with application to the arctic energy balance. University of Alaska, Geophysical Institute Rep., UAG R-307, 193 pp.
- , and K. Jayaweera, 1984: Physical characteristics of arctic stratus clouds. *J. Climate Appl. Meteor.*, **23**, 584–596.
- , and —, and K. Stamnes, 1983: Dependence of radiative properties of arctic stratus clouds on cloud microstructure. *Geophys. Res. Lett.*, **10**, 1188–1191.
- Twomey, S., and C. F. Bohren, 1980: Simple approximations for calculations of absorption in clouds. *J. Atmos. Sci.*, **37**, 2086–2094.
- Valero, F. R. J., T. P. Ackerman and W. J. Y. Gore, 1983: Radiative effects of the arctic haze. *Geophys. Res. Lett.*, **10**, 1184–1187.
- van de Hulst, 1957: *Light Scattering by Small Particles*. Wiley, 470 pp.
- Vowinckel, E., and S. Orvig, 1970: The climate of the north polar basin. *World Survey of Climatology*, vol. 14, *Climates of the Polar Regions*, Elsevier, 129–252.
- Warren, S. G., 1982: Optical properties of snow. *Rev. Geophys. Space Phys.*, **20**, 67–89.
- , and W. J. Wiscombe, 1980: A model for the spectral albedo of snow. II: Snow containing atmospheric aerosols. *J. Atmos. Sci.*, **37**, 2734–2745.
- , C. J. Hahn, J. London, R. M. Chervin and R. L. Jenne, 1988: Global distribution of total cloud cover and cloud type amounts over the ocean. NCAR Tech. Note.
- Welch, R. M., S. K. Cox and J. M. Davis, 1980: Solar radiation and clouds. *Meteor. Monogr.*, **39**, 96 pp.
- Wiscombe, W. J., 1975: Solar radiation calculations for arctic summer stratus conditions. *Climate of the Arctic*, G. Weller and S. Bowling, Eds., University of Alaska Press, 436 pp.
- , 1976: On initialization, error and flux conservation in the Doubling method. *J. Quant. Spectrosc. Radiat. Transfer*, **16**, 637–658.
- , and J. W. Evans, 1977: Exponential-sum fitting of radiative transmission functions. *J. Comput. Phys.*, **24**, 416–444.
- , and S. G. Warren, 1980: A model for the spectral albedo of snow. I: Pure snow. *J. Atmos. Sci.*, **37**, 2712–2733.
- , R. M. Welch and W. D. Hall, 1984: The effects of very large drops on cloud absorption. Part I: Parcel models. *J. Atmos. Sci.*, **41**, 1336–1355.